

g-C₃N₄ with tunable affinity and sieving effect endowing polymeric membranes with enhanced CO₂ capture property

Long Cheng¹, Guozhen Liu¹, Yangyang Mao², Gongping Liu², and Wanqin Jin¹

¹Nanjing University of Technology

²Nanjing Tech University

May 5, 2020

Abstract

g-C₃N₄ nanosheets with tunable CO₂ adsorption properties and nanostructures were synthesized and incorporated into polyether block amide (Pebax) membrane for CO₂ separation. The g-C₃N₄ nanosheets with variable adsorption properties were produced from two monomers, dicyandiamide and melamine, and the variation of nanostructures was controlled by thermal oxidation etching process. The effects of CO₂-philic and molecular sieving properties of g-C₃N₄ nanosheets on solubility and diffusivity of gas molecules in the as-prepared membranes were systematically investigated. The results demonstrated that the g-C₃N₄ nanosheets produced from dicyandiamide and undergoing 4 h thermal etching (DCN-4 nanosheets) showed the optimal CO₂ sorption and sieving property. The membrane with 0.25 wt% DCN-4 nanosheets exhibited simultaneous enhancement in CO₂ permeance and CO₂/N₂ selectivity compared with pure Pebax membrane. Moreover, the membrane maintained its separation performance during long-term operation test, showing great potential for CO₂ capture.

Introduction

Two-dimensional (2D) materials, such as graphene oxide (GO), MXene and metal-organic framework (MOF) nanosheets, have been emerging stars in condensed matter physics, material science and chemistry¹⁻⁵. The atomic thickness of 2D materials can minimize the transport resistance, and the sub-nanometer inherent pores or interlayer channels can provide fast and selective pathways for small molecules, which enables them excellent nano-building blocks for membranes with distinct laminar structure and tunable physicochemical properties⁶⁻¹⁰. Typically, GO has been widely investigated in gas separation membranes^{11,12}. Li et al. fabricated an ultrathin (~1.8 nm) GO membrane with high H₂/CO₂ and H₂/N₂ selectivity¹³. Wang et al. proposed crosslinking the GO nanosheets with CO₂-facilitated transport carrier (borate), and the resulting membranes exhibited CO₂ permeance up to 650 GPU and CO₂/CH₄ selectivity of 75¹⁴. In our previous work, GO nanosheets were assembled into laminar structures with molecular sieving interlayer spaces and straight diffusion pathways in the polymer environment¹⁵. The as-fabricated membranes exhibited excellent CO₂-selective permeation performance with CO₂ permeability of 100 Barrer and CO₂/N₂ selectivity up to 91.

Graphitic carbon nitride (g-C₃N₄), which possesses a graphite-like layered structure with tri-s-triazine units connected by amino groups in plane and weak van der Waals force between layers. It is a new 2D-material family member for fabricating high-performance membranes^{16,17}. Firstly, the interlayer spaces between g-C₃N₄ nanosheets can provide fast transport channels for small molecules. Wang et al. elaborately assembled the partially exfoliated g-C₃N₄ nanosheets into laminar membrane and demonstrated fast water transport in the self-supported nanochannels¹⁸. Xu and co-workers intercalated molecules with SO₃H and benzene moieties into g-C₃N₄ layers to break up the tightly stacking structure of the laminates¹⁹, leading to two orders of magnitude higher water permeances without sacrificing the separation efficiency. Apart from the interlayer channels, intrinsic nanopores with geometric diameter of ~3.11 Å were distributed on the surface

of g-C₃N₄ nanosheets, providing additional transport pathways and sieving property²⁰. Jiang and co-workers employed the nanopores of g-C₃N₄ nanosheets to promote the selective transport of water molecules (2.6 Å)²⁰ and hydrogen molecules (2.8 Å)²¹ through polymeric membrane. To the best of our knowledge, g-C₃N₄ nanosheet has not been employed for CO₂ separation, probably because the intrinsic nanopores are thought to be difficult for the transport of CO₂ molecules (3.3 Å). Nevertheless, it was reported that slightly larger structural defects with the size of 3.1~3.4 Å (Figure 1) can be generated at the terminal sites of uncondensed NH and NH₂ groups during thermal-condensation synthesis process of g-C₃N₄^{22,23}. The size of such defects could lie at the cut-off between the kinetic diameters of CO₂ (3.3 Å) and N₂ (3.64 Å) molecules and thus enhance CO₂/N₂ sieving property. Moreover, the rich amine groups distributed on the nanosheets can form strong affinity to CO₂ molecules, which is beneficial to the selective transport of CO₂ molecules^{24,25}.

In this work, for the first time, g-C₃N₄ was introduced as building blocks for CO₂ separation. The affinity and transport channels of g-C₃N₄ nanosheets were tuned by varying sintered monomers and controlling thermal oxidation process. The carefully tuned nanosheets were incorporated into Pebax matrix to fabricate membrane for CO₂/N₂ separation. As shown in Figure 1, the g-C₃N₄ nanosheets with the CO₂-philic and sieving properties are expected to enhance the preferential sorption and diffusion of CO₂ over N₂ through the membrane. By controlling the synthesis conditions of nanosheets, including sintering monomer and thermal etching time studied here, the CO₂ affinity and molecular sieving property of the g-C₃N₄ can be further tuned, thereby realizing the simultaneous enhancement of CO₂ permeance and CO₂/N₂ selectivity in the membrane.

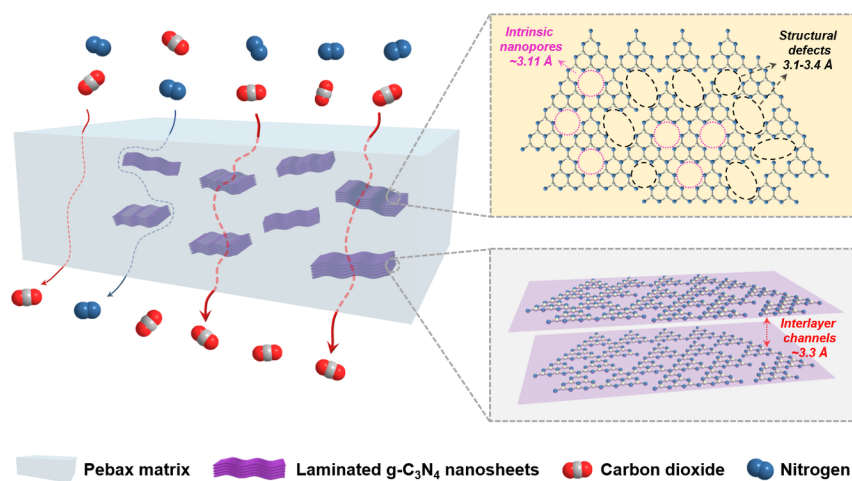


Figure 1. Schematic of the structures of g-C₃N₄ nanosheets, g-C₃N₄-incorporated Pebax MMM and possible gas transport pathways through the membrane.

Experimental

Materials and methods

Dicyandiamide and melamine were obtained from Sigma-Aldrich, Co. and Shanghai Macklin Biochemical Co., Ltd., respectively. Isopropanol was provided by Sinopharm Chemical Reagent Co., Ltd. Pebax 1657 was bought from Arkema, France. The polyacrylonitrile (PAN) ultrafiltration membrane (molecular weight cut-off: 100 kDa) with the flat-sheet configuration was purchased from Shandong Megavision Membrane Technology & Engineering Co., Ltd., China. Gases of N₂, CO₂ and Ar with purity 99.999% were purchased from Nanjing Special Gases Company. Deionized water was used in all the experiments. All of the materials were used without further purification.

g-C₃N₄ synthesis

Bulk $g\text{-C}_3\text{N}_4$ powders were obtained by sintering different monomers, dicyandiamide and melamine, which were referred to as dicyandiamide-sintered $g\text{-C}_3\text{N}_4$ (DCN) and melamine-sintered $g\text{-C}_3\text{N}_4$ (MCN). The DCN powder was synthesized as described in Cheng's work²⁶. In detail, a certain amount of dicyandiamide was heated to 550 °C at a ramp rate of 2.3 °C/min, followed by a thermostatic period of 4 h in static air. Then the cooling rate was controlled at around 1 °C/min. The collected yellow agglomerates were milled into powder in a mortar. The MCN powder was synthesized by replacing dicyandiamide with melamine according to the same procedure.

The thermal oxidation etching method combined with sonication was employed to prepare $g\text{-C}_3\text{N}_4$ nanosheets. As described in literature²⁶, 400 mg DCN or MCN powders were placed in an open ceramic container, which was heated at 500 °C for 2 h, 4 h or 6 h with a ramp rate of 5 °C/min to obtain nanosheets with different exfoliation extents. The nanosheets were then sonicated in the mixed solvent of water and isopropanol (IPA) (1:1, volume ratio), followed by a purification step of centrifugation at 4000 rpm for 1 h. The supernatant was collected and freeze-dried to obtain the final product. The as-prepared nanosheets were referred as DCN-X or MCN-X, where X represents the time (h) of thermal-etching process. It should be noted that DCN-2, DCN-4 and DCN-6 nanosheets were also referred to as multi-layer, few-layer and porous $g\text{-C}_3\text{N}_4$ nanosheets respectively according to their intrinsic morphologies.

Membrane preparation

At first, a certain amount of $g\text{-C}_3\text{N}_4$ nanosheets was dissolved in the mixture solvent of ethanol and water (7:3, volume ratio) by mild sonication. Then Pebax was added into the solution, followed by stirring at 80 °C for 12 h with a condenser tube to avoid solvent volatilization. The mass percentage of $g\text{-C}_3\text{N}_4$ in the membrane was measured as follows:

which was controlled at 0.125 %, 0.25 %, 0.5 %, 1.0 % and 2.0 % to fabricate membranes with different loadings. The casting solution was spinning coated on the PAN substrate at 1000 rpm to fabricate composite membranes. In addition, the freestanding membrane samples were also fabricated by dish casting method for characterization. The as-prepared membranes were firstly dried at room temperature for 24 h, followed by vacuum drying at 80 °C for 24 h to sufficiently remove the residual solvents. The $g\text{-C}_3\text{N}_4$ nanosheets produced from different monomers (DCN-4 and MCN-4) or those undergoing different times of thermal-etching (DCN-2 and DCN-6) were respectively employed to prepare $g\text{-C}_3\text{N}_4$ /Pebax MMMs by the same procedure as mentioned.

Characterizations

The lateral size and thickness of $g\text{-C}_3\text{N}_4$ nanosheets were measured by atomic force microscopy (AFM, Bruker ICON, USA) operated in the tapping mode. The morphology of $g\text{-C}_3\text{N}_4$ nanosheets and membranes was observed by field emission scanning electron microscopy (FESEM, S4800, Hitachi Limited, Japan) and transmission electron microscope (TEM, JEM-2100F, Japan Electron Optics Laboratory Co., Ltd., Japan). X-ray diffraction (XRD, Smartlab 3kW, Rigaku, Japan) was employed to characterize and compare the crystal phases of $g\text{-C}_3\text{N}_4$ nanosheets prepared under different conditions. The scan range was set as 5 ° [?] 2θ [?] 40 ° with a step width of 0.05 ° and a scan rate of 0.2 s step⁻¹ at room temperature. The element compositions of $g\text{-C}_3\text{N}_4$ nanosheets were analyzed by X-ray photoelectron spectroscopy (XPS, Thermo ESCALAB 250, USA). Fourier transform infrared spectra (FTIR, Thermo, Nicolet Nexus 470 spectrometer, USA) was employed to characterize the functional groups of $g\text{-C}_3\text{N}_4$ samples in the range of 500-4000 cm⁻¹. Thermal gravimetry analysis (TGA, NETZSCH STA 449F3) was performed under N₂ to investigate the thermal properties of $g\text{-C}_3\text{N}_4$ nanosheets and the membranes in the range of 50-1000 °C with a ramp rate of 10 °C/min. BET surface areas of bulk powders and nanosheets were calculated from N₂ adsorption isotherms (77 K) measured by TriStar II 3flex (Micromeritics, USA). Gas adsorption experiments of $g\text{-C}_3\text{N}_4$ nanosheets and membranes at 25 °C were measured by BELSOPR-HP (MicrotracBEL Corp., Japan) with N₂ and CO₂.

Gas permeation measurements

During the pure gas and mixed gas permeation tests, a constant pressure/variable volume technique was

employed to test the membrane separation performance. The testing pressure and temperature were set as 0.3 MPa and 25 °C for pure gas permeation test. When the system reached steady-state, the gas permeance P was calculated from the average value of at least three test results calculated by the following equation:

where P represents the gas permeance ($1 \text{ GPU} = 10^{-6} \text{ cm}^3 (\text{STP}) \text{ cm}^{-2} \text{ s}^{-1} \text{ cmHg}$), p_{atm} represents the atmospheric pressure (atm), Δp and T refers to the transmembrane pressure (atm) and the testing temperature (°C) respectively, A is the effective area of membrane, and dV/dt corresponds to the volumetric displacement rate in the bubble flow meter. The ideal selectivity α of CO_2/N_2 was calculated by the ratio of the permeance of the individual gases which can be expressed as follows:

For the mixed gas permeation test, the total flux of the gas mixture (CO_2 : N_2 , 50 vol%: 50 vol%) was controlled at 60 mL min^{-1} , while Ar was chosen as the sweep gas with a flux of 10 mL min^{-1} (Supporting Information Figure S1). The mixed gas permeation test was carried out at total pressure of 0.3 MPa and 25 °C. The component of the mixed gas was detected by gas chromatography (Agilent 7820A, USA). The selectivity of binary gas mixtures can be calculated as follows:

where x and y represent the volumetric fractions of the one component in the feed and permeate side, respectively.

Results and discussion

Synthesis of g- C_3N_4 nanosheets by thermal-etching process

At first, the thermal-etching process of dicyandiamide-sintered g- C_3N_4 (DCN) was investigated. To verify the efficiency of the thermal-etching method, the morphologies of DCN powders before and after the etching process were compared by SEM characterizations. As we can see from Figure 2a, the size of pristine DCN powders was 1-2 μm , and the laminar structure can be observed at higher magnification. After thermal etching of 4 h, the morphology of powders was transformed into sheet-like structure (Figure 2b).

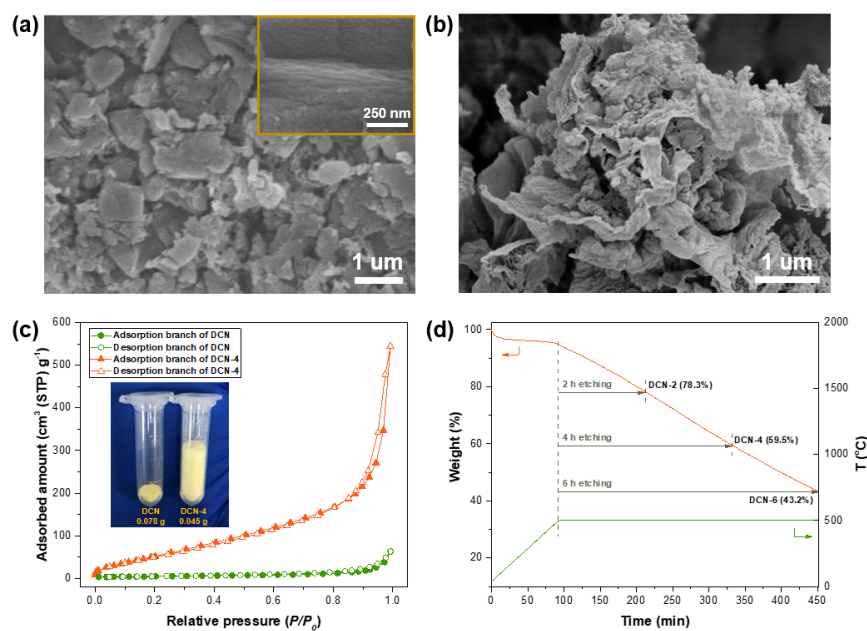


Figure 2. SEM images of (a) bulk DCN powders and (b) DCN-4 nanosheets obtained after thermal-etching process, and the inset in (a) is the bulk powder with higher magnification. (c) N_2 adsorption isotherms (77 K) of DCN and DCN-4 samples; the inset is the digital photos of two kinds of powders. (d) TGA curve of DCN powders with a constant temperature period of 6 h at 500 °C.

The product obtained from thermal-etching method was then dispersed in IPA/water mixed solvent and sonicated to exfoliate the nanosheets into solvents, which was further centrifuged for purification, followed by the freeze-drying process to prepare the nanosheets. From the N_2 adsorption isotherms of DCN powder and DCN-4 nanosheets, the N_2 adsorption amount of DCN-4 nanosheets was greatly improved to 544 cm^3 (STP) g^{-1} , and the Brunauer-Emmett-Teller (BET) surface area was increased from 17.8 to $252.1 \text{ m}^2\text{g}^{-1}$, reflecting the successful exfoliation of bulk $g\text{-C}_3\text{N}_4$ powders into nanosheets. Besides, the isotherm of DCN-4 nanosheets can be identified as type II with H4-type hysteresis loop on the basis of the IUPAC classification, which was attributed to the slit-like pores generated from the aggregation of nanosheets during the freeze-drying^{27,28}. In addition, the digital photos also showed the volume of powders obviously expanded after the exfoliation, which further verified the efficiency of the thermal etching method. To investigate the mass change during the thermal-etching process, the DCN powder was characterized by TGA under the same condition for thermal-etching process (Figure 2d). The initial slight weight loss was attributed to the loss of uptake water. After the temperature reached 500°C , the layer-by-layer thermal oxidation etching started²⁶. With the bulk $g\text{-C}_3\text{N}_4$ powder successively going through 2 h, 4 h and 6 h thermal oxidation, the weight loss was almost linearly to the soaking time, finally dropping to 43.2 % by etching for 6 h. By controlling the etching time, the morphologies and physico-chemical properties of $g\text{-C}_3\text{N}_4$ can be effectively tuned, which will be later discussed in detail.

The light white $g\text{-C}_3\text{N}_4$ solution obtained after centrifugation exhibits a Tyndall effect due to light scattering of exfoliated $g\text{-C}_3\text{N}_4$ nanosheets in the solution (Figure 3a). High-resolution TEM was employed to further characterize the morphology of nanosheets. As shown in Figure 3b, the nanosheet was very thin that the underneath copper net can be clearly observed. In addition, the rich graphene-like wrinkles on the surface were shown as well, which was consistent with literature²¹. Moreover, the elemental composition of the as-prepared nanosheets was detected by XPS analysis. Figure 3c showed that the $g\text{-C}_3\text{N}_4$ nanosheets are high purity which are mainly composed of C and N elements, and the tiny amount of oxygen element can be ascribed to the tiny amount of O_2 adsorbed on the surface of the synthetic product during polymerization process²⁹. In addition, the molar ratio of N/C for the as-prepared $g\text{-C}_3\text{N}_4$ nanosheets is ~ 1.39 , which is very close to the stoichiometric ratio of $g\text{-C}_3\text{N}_4$ (~ 1.33). There were two peaks at 288.5 and 284.8 eV in the C1s spectrum, which corresponded to the sp^2 -bonded carbon and the standard reference carbon, respectively^{29,30}. As we can see in the N 1s spectrum, the dominant peak at 398.8 eV was attributed to the sp^2 -bonded nitrogen in triazine rings ($\text{C-N}=\text{C}$), while the peaks at 399.5, 400.9 and 404.5 eV could be ascribed to the bridging N atoms in $\text{N}(\text{-C})_3$, the terminal amino groups and π -excitations, respectively^{18,31}.

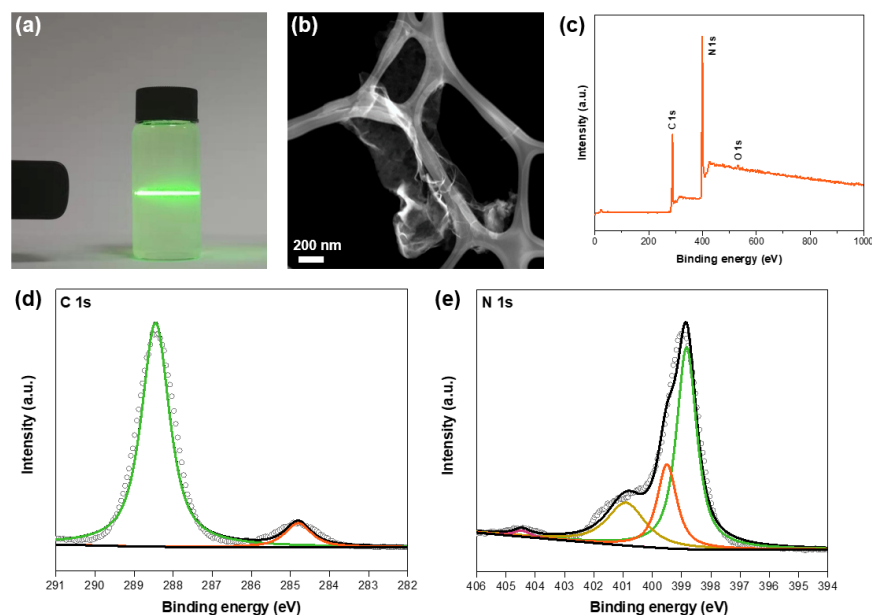


Figure 3. (a) Digital photographs of the DCN-4 nanosheets dispersed in the mixed solvent of IPA/water (1:1, volume ratio) with the concentration of 0.1 mg/mL. The green laser was used to exhibit the Tyndall effect. (b) TEM images of the ultrathin DCN-4 nanosheet. (c) XPS spectrum of the g-C₃N₄ nanosheets. High-resolution XPS spectra of (d) C 1s and (e) N 1s of the DCN-4 nanosheets.

g-C₃N₄ nanosheets with tunable nanostructures and physico-chemical properties

During the exploration of the synthesis of g-C₃N₄ nanosheets, we found that the selection of different monomers for sintering g-C₃N₄ powders would significantly affect the physico-chemical property of the as-prepared nanosheets, especially the gas adsorption property. Two kinds of monomers, dicyandiamide and melamine, were respectively chosen for sintering bulk g-C₃N₄ and preparing corresponding nanosheets (DCN-4 and MCN-4). Firstly, the crystal phases of the as-prepared nanosheets were investigated by XRD patterns (Figure 4a). The characteristic peaks ((1 0 0) and (0 0 2)) of DCN-4 and MCN-4 patterns occurred at 13.0° and 27.6°, which were assigned to the in-plane triangular nanopores and the graphite-like laminar structure, respectively¹⁹. The variation of functional groups between monomers and nanosheets was characterized by FTIR (Figure 4b). The peaks from 3000 to 3650 cm⁻¹ corresponded to the stretching vibrations of -NH- or -NH₂ groups^{32,33}. The transformation into broad peaks in patterns of nanosheets was attributed to the polymerization reaction of amino groups during the sintering process. In addition, the stronger peak at 3167 cm⁻¹ in DCN-4 than that in MCN-4 indicated more amino groups existing at the terminal defect sites of DCN-4 nanosheets, which would provide higher CO₂ affinity. The vibrations of N-(C)₃ and -NH- occurred at 1200-1750 cm⁻¹²¹, which could be observed in all patterns of monomers and nanosheets. Comparing the FTIR patterns of dicyandiamide and DCN-4 nanosheets, the peak corresponding to the characteristic C[?]N bonds at 2165 cm⁻¹ disappeared and a new peak of heptazine units occurred at 813 cm⁻¹, confirming the polymerization of dicyandiamide into g-C₃N₄^{22,33}. Besides, the peaks at the same wavenumber of 813 cm⁻¹ in FTIR patterns of melamine and MCN-4 corresponded to triazine and heptazine units, respectively^{22,34}.

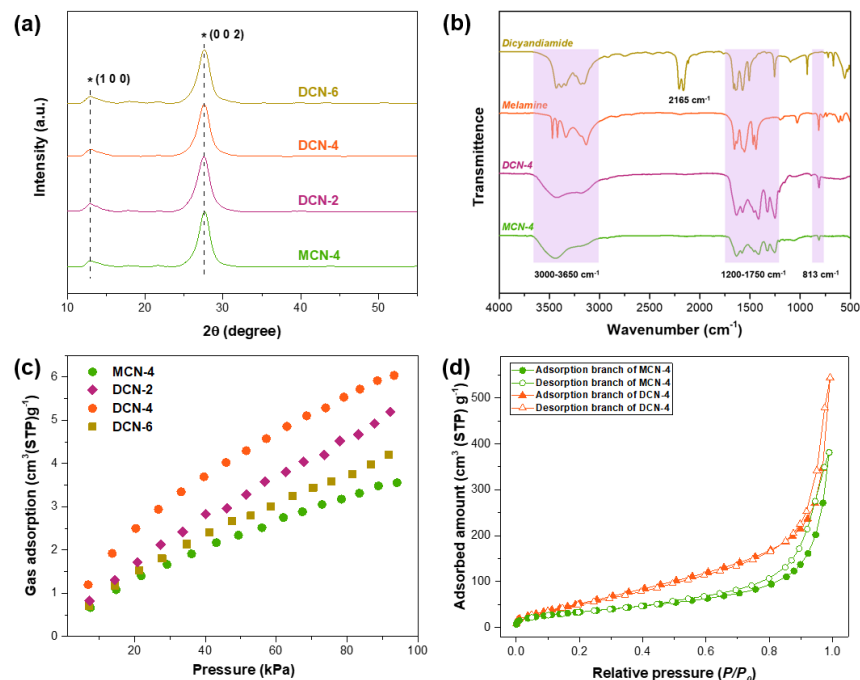


Figure 4. (a) XRD patterns of MCN-4, DCN-2, DCN-4 and DCN-6 nanosheets. (b) FTIR patterns of two monomers (dicyandiamide and melamine) and resulting nanosheets (DCN-4 and MCN-4). (c) CO₂ adsorption isotherms of MCN-4, DCN-2, DCN-4 and DCN-6 nanosheets at 25 °C. (d) N₂ adsorption isotherms (77 K) of MCN-4 and DCN-4 nanosheets.

TGA curves (Supporting Information Figure S2) of DCN-4 and MCN-4 nanosheets demonstrated both nanosheets were thermally stable higher than 500 °C. CO₂ adsorption isotherms of these two nanosheets were measured to explore the differences in adsorption properties. Figure 4c showed that the CO₂ adsorption amount of DCN-4 nanosheets was 70% higher than that of MCN-4 at ~1 bar, which was consistent with the more amino groups in DCN-4 observed in FTIR patterns. This would affect the CO₂ adsorption of as-prepared membrane and thus the separation performance. Moreover, the N₂ adsorption isotherms (77 K) of MCN-4 and DCN-4 nanosheets were compared in Figure 4d. The isotherm of MCN-4 was type II with H4-type hysteresis loop as well, which was similar to that of DCN-4. However, the BET surface area of MCN-4 nanosheets was 126.7 m²/g, which was only half of that of DCN-4 (252.1 m²/g), which might be caused by the different polymerization processes of the two monomers. Therefore, sintering monomers with different molecular structures can produce g-C₃N₄ nanosheets with tunable CO₂ affinity, which would endow the membrane with variable solubility and thus gas transport properties.

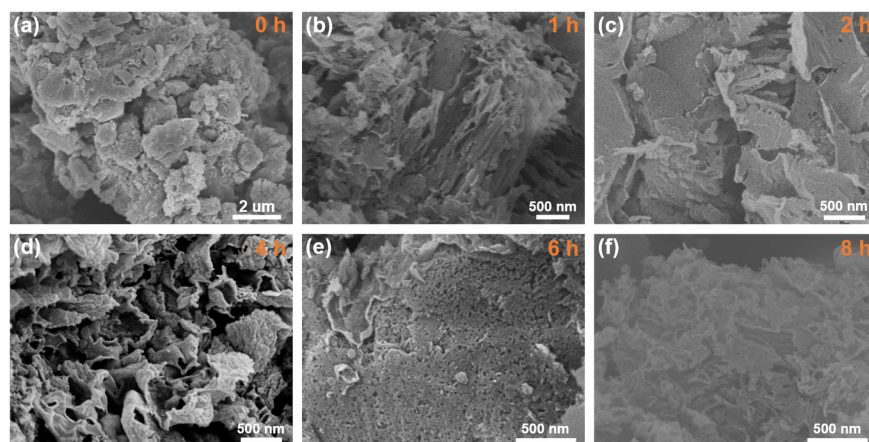


Figure 5. SEM images of DCN powders obtained after different times (0~8 h) of thermal-etching process.

Apart from the effect of sintered monomers on the preferential sorption of nanosheets, we explored the effect of thermal etching time on the nanostructures of the nanosheets as well. DCN powders treated by different thermal-etching times (1 h, 2 h, 4 h, 6 h and 8 h) were characterized by SEM. Figure 5 showed the pristine DCN powder exhibited the bulk morphology with lateral size of 1~2 μm . After 1 h thermal etching, the nanosheets began to emerge like flower-blooming from the edges of bulk powders. When it came to 2 h, a few nanosheets were exfoliated. As we can see from Figure 5d, large amounts of thinner $\text{g-C}_3\text{N}_4$ nanosheets with few defects could be obtained after 4 h thermal-etching, which was beneficial to fabricating high-quality membranes¹¹. Large amounts of nanopores were clearly observed after 6 h of etching, which would promote gas transport rate but reduce sieving property. Further extending the time to 8 h could excessively corrode the nanosheets into little fragments, losing the typical 2D structure of $\text{g-C}_3\text{N}_4$ (Figure 5f).

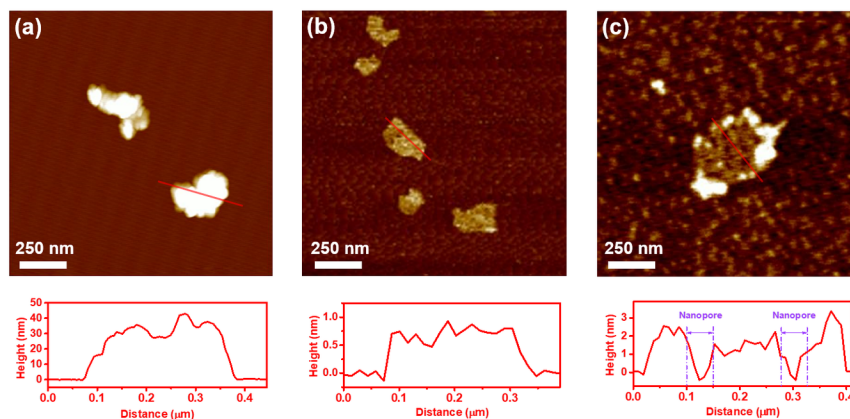


Figure 6. AFM images and the corresponding height profiles of (a) DCN-2, (b) DCN-4 and (c) DCN-6 nanosheets.

AFM was used to further study the morphologies of typical $\text{g-C}_3\text{N}_4$ nanosheets (DCN-2, DNC-4 and DCN-6). As we can see in Figure 6, all the nanosheets with different degrees of corrosion exhibited the similar lateral size of 300~400 nm. Nevertheless, the thickness and the distribution of nanopores on the nanosheets differed from each other. The thickness of DCN-2 nanosheets was about 30 nm, which was relatively thick, resulting from the insufficient exfoliation of 2 h thermal-etching. Therefore, the DCN-2 nanosheets were referred to as multi-layer $\text{g-C}_3\text{N}_4$ nanosheets. This kind of multi-layer nanosheets would partially improve the transport

resistance, leading to the decreased gas permeance. When it came to 4 h, the thickness of nanosheets was reduced to ~ 1 nm. Compared with the multi-layer $g\text{-C}_3\text{N}_4$ nanosheets, these few-layer $g\text{-C}_3\text{N}_4$ nanosheets are preferred to fabricate high-performance membranes due to the relatively low resistance and the structural defects for molecular sieving. In addition, the interlayer space between nanosheets can provide additional transport channels as well. However, excessive thermal etching of 6 h would produce lots of nanopores with size of ~ 50 nm in the DCN-6 nanosheets (here considered as porous $g\text{-C}_3\text{N}_4$ nanosheets), which could be observed from both SEM and AFM images (Figures 5e and 6c). On one hand, the nanopores would reduce the transport resistance and improve the gas permeation rate. On the other hand, the molecular sieving property would decline because of the larger pore size. The results suggested that the nanostructures of the $g\text{-C}_3\text{N}_4$ nanosheets could be efficiently tuned by controlling the thermal-etching time.

The physico-chemical properties of the $g\text{-C}_3\text{N}_4$ nanosheets undergoing different thermal-etching times (DCN-2, DCN-4 and DCN-6) were further characterized by XRD, TGA and gas adsorption test. Figure 4a showed all the nanosheets exhibited the same characteristic peaks corresponding to (1 0 0) and (0 0 2), which were identical to the crystal phases of MCN-4. The DCN nanosheets also exhibited similar thermostability observed in MCN-4 (Supporting Information Figure S2). Nevertheless, the thermal-etching time plays a critical role in the resulting CO_2 adsorption properties of nanosheets. As shown in Figure 4c, 4 h was found to be optimized thermal-etching time to synthesize the DCN nanosheets with highest adsorption capacity (DCN-4). This might be attributed to their distinct morphologies and the amounts of CO_2 -philic amino groups distributed on the nanosheets, which would affect the gas transport through the membrane.

Characterization of $g\text{-C}_3\text{N}_4$ /Pebax membranes

The as-prepared nanosheets were incorporated into the Pebax matrix to fabricate $g\text{-C}_3\text{N}_4$ /Pebax MMMs. Figure 7 showed the freestanding membrane was transparent and exhibited uniform color of light yellow, which was consistent with the powder color, indicating a homogeneous dispersion of nanosheets in the polymer matrix.

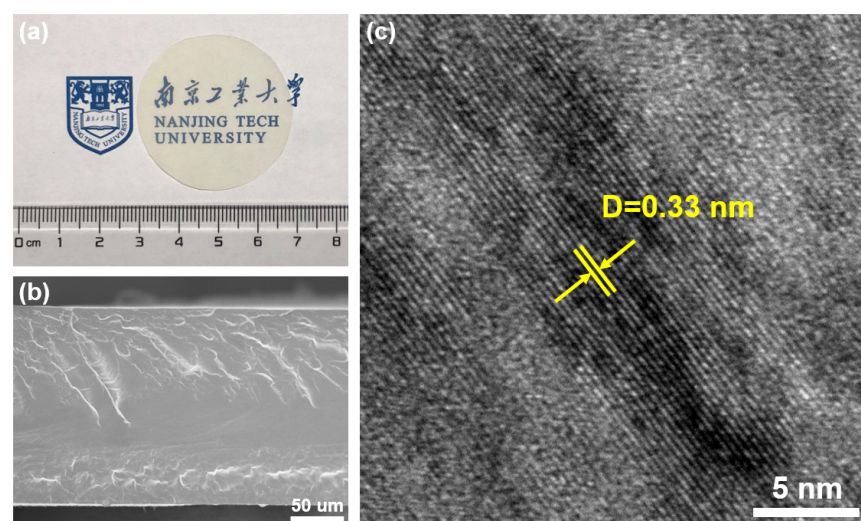


Figure 7. (a) Digital photograph of MMMs with 0.25 wt% DCN-4. (b) SEM image and (c) TEM image of the cross-section of freestanding MMMs. The yellow lines indicate the channel size of the assembled nanosheets.

The cross-section SEM image (Figure 7b) of the freestanding membrane showed an uniform thickness. Porous PAN supported $g\text{-C}_3\text{N}_4$ /Pebax composite membrane was also characterized by SEM (Supporting Information Figure S3). It owned typical smooth and dense surface and the separation layer had good adhesion onto the PAN substrate, while pore penetration occurred, which would partially increase the transport resistance

and reduce the gas permeance. The wrinkled nanosheets could be observed in the active layer, showing good interfacial compatibility with the polymer matrix. TEM image of the nanosheets dispersed in polymer phase further demonstrated that the g-C₃N₄ nanosheets were assembled into laminar structure with the channel height of ~ 3.3 Å (Figure 7c), which was close to the kinetic diameter of CO₂ (3.3 Å) but exceeded that of N₂ (3.64 Å). Therefore, we expected the g-C₃N₄ nanosheets in the Pebax matrix could enhance the sieving property and thus the gas separation performance.

The effect of introducing g-C₃N₄ nanosheets on the membrane physico-chemical property was also characterized by XRD and FTIR. The XRD results (Supporting Information Figure S4) demonstrated that the peak at 27.6° corresponding to (0 0 2) in g-C₃N₄ nanosheets appeared when the loading reached 1.0 wt%, confirming the introduction of nanosheets into Pebax matrix. This peak was undetectable in membranes with relatively low g-C₃N₄ loading because the intensity of the peak was quite low compared with that of the polymer matrix. The FTIR spectra (Supporting Information Figure S5) showed the typical vibrations of functional groups of Pebax¹⁵. The peaks at 1322 and 1415 cm⁻¹ corresponding to the vibrations of N-(C)₃ and C-NH-C from g-C₃N₄ nanosheets were observed in the DCN-4/Pebax membrane²¹, which further verified the successful incorporation of g-C₃N₄ nanosheets into the polymer. The thermal stability of the membrane with different g-C₃N₄ loadings was investigated by TGA curves (Supporting Information Figure S6). There was a one-step weight loss profile at the pyrolysis temperature of 350-450 °C, which was consistent with the decomposition temperature of pure Pebax membrane in literature³⁵. The incorporation of g-C₃N₄ nanosheets had little effect on the thermal stability of membranes due to the quite low loading.

Moreover, the effect of g-C₃N₄ nanosheets on the membrane sorption property was studied by measuring the CO₂ and N₂ sorption isotherms (Figure 8). As expected, the CO₂ sorption capacity in the membrane was improved by introducing the CO₂-philic g-C₃N₄ nanosheets, while the N₂ adsorption was almost unchanged, leading to higher CO₂/N₂ sorption selectivity. For DCN-4-based membranes, the CO₂ sorption amount was gradually increased with adding the loading of DCN-4 nanosheets, which was attributed to the increase of CO₂-philic groups from more g-C₃N₄ nanosheets incorporated into the polymer matrix. Moreover, compared with MCN-4, the DCN-4 nanosheets with higher CO₂ affinity afford the membrane higher CO₂ sorption capacity and CO₂/N₂ sorption selectivity. It was also found that varying the thermal etching time of DCN nanosheets has little influence on the membrane sorption property. The observed variations of sorption property would affect the gas separation performance of the membranes.

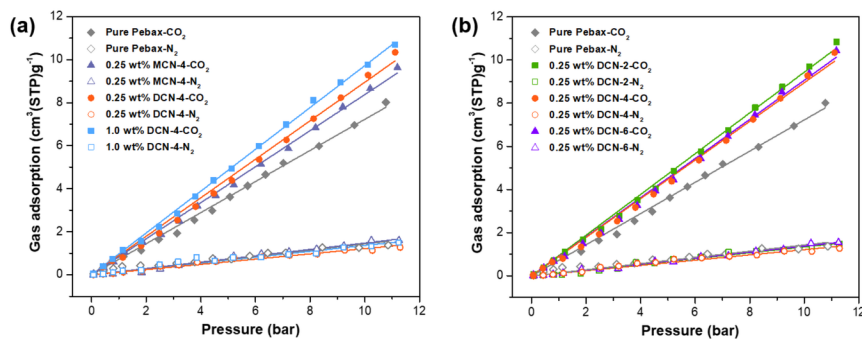


Figure 8. (a) CO₂ and N₂ adsorption isotherms of pure Pebax and g-C₃N₄/Pebax MMM with 0.25 wt% MCN-4 or DCN-4, 1.0 wt% DCN-4 nanosheets at 25 °C. (b) CO₂ and N₂ adsorption isotherms of pure Pebax and g-C₃N₄/Pebax MMM with 0.25 wt% DCN-2, DCN-4 or DCN-6 nanosheets at 25 °C.

Gas transport properties

CO₂/N₂ separation performance was measured to study the effect of g-C₃N₄ nanosheets on transport property of the membrane (Figure 9). It was found that introducing g-C₃N₄ nanosheets with CO₂ preferential sorption and sieving property significantly enhanced the CO₂/N₂ selectivity of Pebax membrane. Moreover,

the DCN-4-based membrane exhibited much higher CO_2/N_2 separation performance than the MCN-4-based membrane, showing enhancement both in permeance and selectivity compared with pure Pebax membrane. Hence, the dicyandiamide-sintered $\text{g-C}_3\text{N}_4$ (DCN) powder was chosen to further investigate the effect of thermal-etching time and nanosheets loading on the gas separation performance.

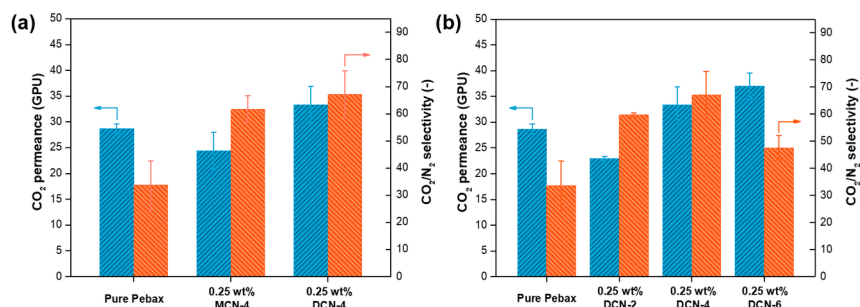


Figure 9. (a) Effect of $\text{g-C}_3\text{N}_4$ nanosheets produced from different monomers on the gas separation performances of MMMs. (b) Effect of $\text{g-C}_3\text{N}_4$ nanosheets obtained after different times of thermal-etching on the gas separation performance of MMMs. The pure gas permeation was measured at 0.3 MPa and 25 °C.

Multi-layer, few-layer and porous $\text{g-C}_3\text{N}_4$ nanosheets, resulted from different thermal etching times (DCN-2, DCN-4 and DCN-6), also determined the membrane separation performance (Figure 9b) which could be attributed to the different transport pathways for gas molecules (Figure 10). Incorporation of multi-layer (DCN-2) or few-layer $\text{g-C}_3\text{N}_4$ (DCN-4) could enhance the CO_2/N_2 selectivity, while few-layer $\text{g-C}_3\text{N}_4$ with much smaller thickness showed lower transport resistance that lead to the increased CO_2 permeance. By contrast, the porous $\text{g-C}_3\text{N}_4$ nanosheets (DCN-6), generated by 6 h thermal etching, endowed the membrane highest permeance whereas lowest selectivity compared with the multi-layer $\text{g-C}_3\text{N}_4$ (DCN-2) and few-layer $\text{g-C}_3\text{N}_4$ (DCN-4) based membranes. This can be attributed to that the excessively large nanopores appearing on the nanosheet (Figure 6c) shortened the gas pathways, but decreased sieving effect of CO_2 over N_2 .

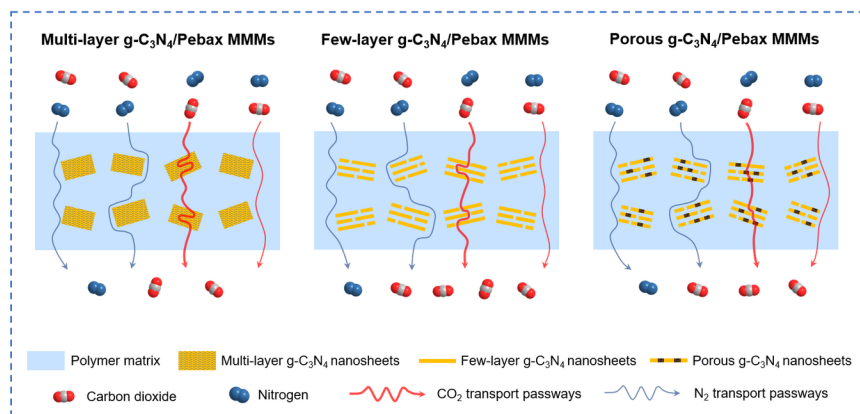


Figure 10. Schematic of the structures of MMMs incorporated with $\text{g-C}_3\text{N}_4$ nanosheets of different morphologies and the corresponding gas transport pathways through the membranes.

According to the solution-diffusion model³⁶, the permeability (P) could be defined as the product of the sorption coefficient (solubility, S) and the diffusion coefficient (diffusivity, D) to further explore the gas transport mechanism through the membrane. The values of S and D for CO_2 and N_2 under the testing condition (0.3 MPa, 25 °C) was determined by the high-pressure adsorption isotherms (Figure 8) and the

measured permeability. The sorption/diffusion coefficients and selectivity were summarized in Figure 11. In general, both the CO₂ sorption coefficient and CO₂/N₂ sorption selectivity of the membrane were improved with the incorporation of g-C₃N₄ nanosheets, which was attributed to the CO₂-philic properties of nanosheets. The membrane diffusion selectivity was improved while the diffusion coefficients were reduced by incorporating g-C₃N₄ nanosheets, which are due to the higher molecular sieving property and transport resistance. As expected, the DCN-4 nanosheets with higher CO₂ affinity endowed the membrane with larger CO₂ sorption coefficient and selectivity compared with MCN-4.

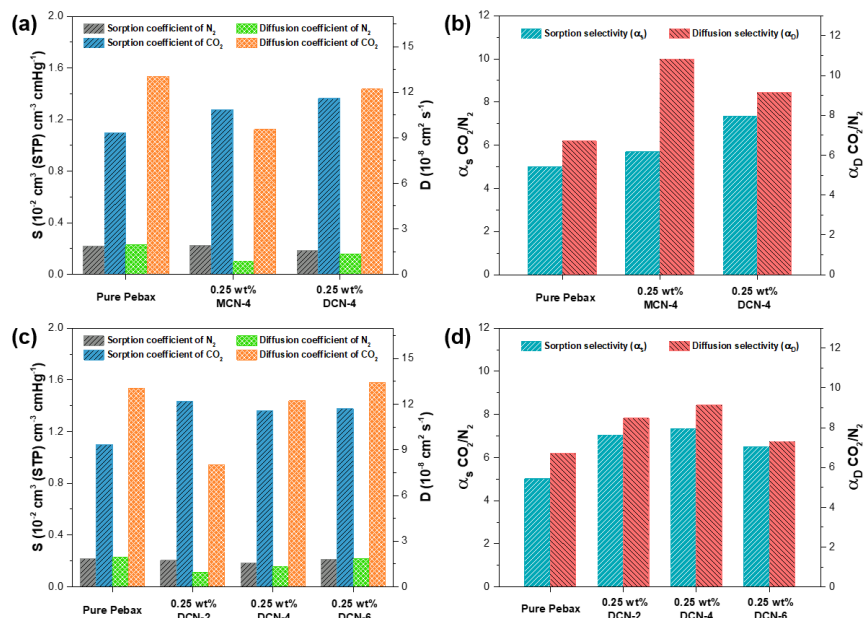


Figure 11. (a) Solubility and diffusivity of CO₂ and N₂, and (b) sorption and diffusion selectivity in pure Pebax membrane, 0.25 wt% MCN-4/Pebax and DCN-4/Pebax membranes. (c) Solubility and diffusivity of CO₂ and N₂, and (d) sorption and diffusion selectivity in pure Pebax membrane, 0.25 wt% DCN-2/Pebax, DCN-4/Pebax and DCN-6/Pebax membranes.

In addition, the effect of g-C₃N₄ nanosheets with different sieving properties on the separation performance was further analyzed by the D-S coefficients and selectivity as well (Figure 11c-d). Overall, the CO₂ sorption coefficients of three kinds of DCN/Pebax membranes were higher than that of pure Pebax membrane, which was in accordance with the adsorption results in Figure 8b. Among them, the sorption selectivity of DCN-4/Pebax membrane was highest owing to the highest CO₂ adsorption of DCN-4 nanosheet (Figure 4c). The diffusion coefficients was dropped at first but then increased with prolonging the thermal-etching time of g-C₃N₄ incorporated into the membrane. It indicated that reducing the thickness or increasing the pore size of the g-C₃N₄ nanosheets could decrease the gas transport resistance through the g-C₃N₄ laminates. Importantly, the diffusion selectivity was improved by introducing g-C₃N₄ nanosheets into the membrane, confirming the enhanced molecular sieving property. Moreover, the few-layer g-C₃N₄ (DCN-4) resulting from mild thermal etching is considered as the optimal molecular sieves, because of its smaller thickness and well-controlled pore size compared with its counterparts DCN-2 and DCN-6, respectively.

The analysis of sorption and diffusion parameters demonstrated that introducing g-C₃N₄ nanosheets generally enhanced both the sorption and diffusion of CO₂ over N₂ through the membrane. Further controlling the synthesis conditions (i.e., sintered monomer and thermal etching time), the CO₂ affinity and molecular sieving property of g-C₃N₄ nanosheets were successfully tuned, thereby maximizing the enhancement of CO₂ permeance and CO₂/N₂ perm-selectivity.

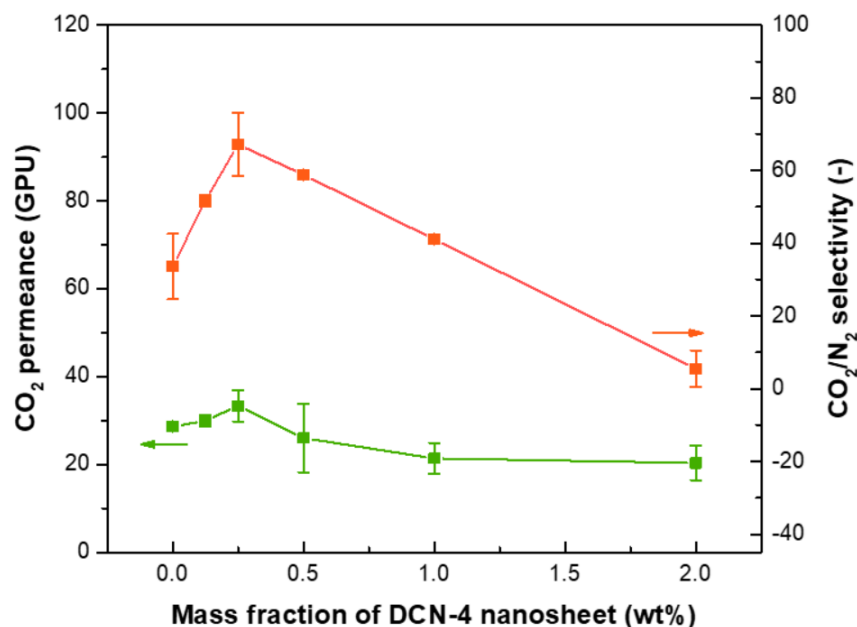


Figure 12. Effect of mass fraction of DCN-4 nanosheet on the CO₂/N₂ separation performance of DCN-4/Pebax MMMs, which was tested at 0.3 MPa and 25 °C.

The CO₂/N₂ separation performances of membranes with different g-C₃N₄ loadings were measured to study the effect of g-C₃N₄ (taking DCN-4 as example) loading on gas transport property. As shown in Figure 12, the CO₂ permeance and CO₂/N₂selectivity were simultaneously improved when the loading increased from 0 to 0.25 wt%. As discussed above, the increase of CO₂permeance was attributed to the improved CO₂preferential sorption and diffusion by incorporating g-C₃N₄ nanosheets. Meanwhile, both the g-C₃N₄ enhanced CO₂/N₂ sorption selectivity and diffusion selectivity contributed to the rising of perm-selectivity. Nevertheless, further adding the loading up to more than 0.5 wt% would greatly decline the separation performance, which is presumably due to the aggregation of nanosheets increasing the transport resistance and resulting in non-selective defects. Hence, the membrane incorporated with 0.25 wt% DCN-4 achieved the optimal CO₂/N₂ separation performance with CO₂ permeance of 33.3 GPU and CO₂/N₂ selectivity of 67.2.

Figure 13a demonstrated the performance stability of the optimized g-C₃N₄/Pebax membrane with finally stable CO₂ permeance of 26 GPU and CO₂/N₂ selectivity of 50 during more than 90 h mixed-gas separation process. Compared with the single gas measurement, the drop of separation performance in mixed gas feed could result from the competitive adsorptions of gas mixtures, which was often found in literature as well³⁷. In addition, the CO₂/N₂ separation performance was compared with Pebax membrane incorporated with various fillers including zeolite^{38,39}, carbon nanotubes^{40,41}, attapulgite⁴², GO^{43,44}, MOFs⁴⁵⁻⁴⁹ and covalent organic frameworks (COFs)^{35,50}. As shown in Figure 13b, our membrane performance is competitive with most of the reported works, offering a potential candidate for CO₂ capture.

It was also noticed that the CO₂ permeance in this work is relatively low in contrast with that of thin-film composite membranes⁵¹⁻⁵³. The main reason lied in the pore penetration at the interface between the separation layer and porous PAN substrate (Supporting Information Figure S3). In the following work, we can employ polydimethylsiloxane (PDMS)⁵⁴ or nanomaterials with diverse dimensions (hydroxide nanofibers⁵⁵ or porous MOF nanosheets⁵⁶) to serve as gutter layers to prevent the pore penetration and further improve the gas permeance.

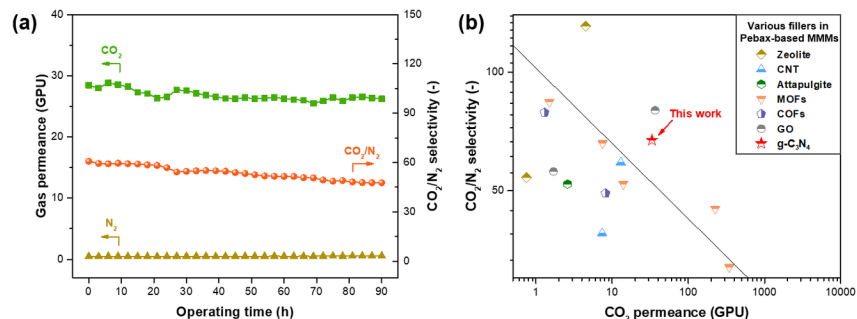


Figure 13. (a) Continuous operation test of the 0.25 wt% DCN-4/Pebax membrane with the feed of mixed gas (CO_2/N_2 , 50 vol%:50 vol%) at 0.3 MPa and 25 °C. (b) Comparison of CO_2/N_2 separation performance of the as-prepared $\text{g-C}_3\text{N}_4$ /Pebax MMMs with those of other Pebax-based MMMs with different kinds of fillers. The corresponding data and references were listed in Supporting Information Table S1.

Conclusion

In this work, CO_2 -philic $\text{g-C}_3\text{N}_4$ nanosheets with tunable preferential sorption and sieving effect were synthesized by thermal oxidation etching and incorporated into Pebax membrane to enhance the CO_2/N_2 separation performance. Different monomers including dicyandiamide and melamine were employed for sintering bulk $\text{g-C}_3\text{N}_4$ and the resulting nanosheets exhibited variable adsorption properties, thereby determining the membrane sorption property and thus separation performance. It was also demonstrated that the nanostructures (thickness and pores) of $\text{g-C}_3\text{N}_4$ nanosheets could be facily tuned by controlling the duration of thermal oxidation etching. The resulting differences in CO_2 sorption and molecular sieving property of $\text{g-C}_3\text{N}_4$ nanosheets endowed the membrane with district sorption and diffusion coefficients, which remarkably enhanced the separation performance as well. The optimized $\text{g-C}_3\text{N}_4$ -based membrane (0.25 wt% DCN-4/Pebax) exhibited good CO_2/N_2 separation performance with CO_2 permeance of 33.3 GPU and high CO_2/N_2 selectivity up to 67.2, which was increased by 100% compared with that of pure Pebax membrane. The proposed approach tuning the nanostructures and physico-chemical properties of $\text{g-C}_3\text{N}_4$ nanosheets is expected to pave an alternative avenue to the design of 2D-material-based membranes for gas separation.

Declaration of competing interest

None.

Acknowledgements

This work was financially supported by the National Natural Science Foundation of China (21776125, 21922805, 91934303, 51861135203), the Innovative Research Team Program by the Ministry of Education of China (grant No. IRT_17R54) and the Topnotch Academic Programs Project of Jiangsu Higher Education Institutions (TAPP).

Literature Cited

1. Dubertret B, Heine T, Terrones M. The Rise of Two-Dimensional Materials. *Accounts Of Chemical Research*. Jan 2015;48(1):1-2.
2. Tan C, Cao X, Wu X-J, et al. Recent Advances in Ultrathin Two-Dimensional Nanomaterials. *Chemical Reviews*. May 10 2017;117(9):6225-6331.
3. Xu M, Liang T, Shi M, Chen H. Graphene-Like Two-Dimensional Materials. *Chemical Reviews*. May 2013;113(5):3766-3798.
4. Geim AK, Grigorieva IV. Van der Waals heterostructures. *Nature*. Jul 25 2013;499(7459):419-425.
5. Geim AK, Novoselov KS. The rise of graphene. *Nature Materials*. Mar 2007;6(3):183-191.

6. Ding L, Wei Y, Li L, et al. MXene molecular sieving membranes for highly efficient gas separation. *Nature communications*. 2018;9(1):155.
7. Huang H, Ying Y, Peng X. Graphene oxide nanosheet: an emerging star material for novel separation membranes. *Journal Of Materials Chemistry A*. 2014 2014;2(34):13772-13782.
8. Liu G, Jin W, Xu N. Two-Dimensional-Material Membranes: A New Family of High-Performance Separation Membranes. *Angewandte Chemie-International Edition*. Oct 17 2016;55(43):13384-13397.
9. Ding L, Wei Y, Wang Y, Chen H, Caro J, Wang H. A two-dimensional lamellar membrane: MXene nanosheet stacks. *Angewandte Chemie International Edition*. 2017;56(7):1825-1829.
10. Wu X, Cui X, Wu W, Wang J, Li Y, Jiang Z. Elucidating Ultrafast Molecular Permeation through Well-Defined 2D Nanochannels of Lamellar Membranes. *Angewandte Chemie*. 2019;131(51):18695-18700.
11. Kim S, Wang H, Lee YM. 2D Nanosheets and Their Composite Membranes for Water, Gas, and Ion Separation. *Angewandte Chemie International Edition*. 2019.
12. Cheng L, Liu G, Jin W. Recent Progress in Two-dimensional-material Membranes for Gas Separation. *Acta Physico-Chimica Sinica*. 2019 2019;35(10):1090-1098.
13. Li H, Song Z, Zhang X, et al. Ultrathin, Molecular-Sieving Graphene Oxide Membranes for Selective Hydrogen Separation. *Science*. Oct 4 2013;342(6154):95-98.
14. Wang S, Wu Y, Zhang N, et al. A highly permeable graphene oxide membrane with fast and selective transport nanochannels for efficient carbon capture. *Energy & Environmental Science*. 2016 2016;9(10):3107-3112.
15. Shen J, Liu G, Huang K, Jin W, Lee K-R, Xu N. Membranes with Fast and Selective Gas-Transport Channels of Laminar Graphene Oxide for Efficient CO₂ Capture. *Angewandte Chemie-International Edition*. Jan 7 2015;54(2):578-582.
16. Wang X, Maeda K, Thomas A, et al. A metal-free polymeric photocatalyst for hydrogen production from water under visible light. *Nature Materials*. Jan 2009;8(1):76-80.
17. Zhang J, Chen Y, Wang X. Two-dimensional covalent carbon nitride nanosheets: synthesis, functionalization, and applications. *Energy & Environmental Science*. 2015 2015;8(11):3092-3108.
18. Wang Y, Li L, Wei Y, et al. Water Transport with Ultralow Friction through Partially Exfoliated g-C₃N₄ Nanosheet Membranes with Self-Supporting Spacers. *Angewandte Chemie-International Edition*. Jul 24 2017;56(31):8974-8980.
19. Ran J, Pan T, Wu Y, et al. Endowing g-C₃N₄ Membranes with Superior Permeability and Stability by Using Acid Spacers. *Angewandte Chemie (International ed. in English)*. 2019-Nov-11 2019;58(46):16463-16468.
20. Cao K, Jiang Z, Zhang X, et al. Highly water-selective hybrid membrane by incorporating g-C₃N₄ nanosheets into polymer matrix. *Journal Of Membrane Science*. Sep 15 2015;490:72-83.
21. Tian Z, Wang S, Wang Y, et al. Enhanced gas separation performance of mixed matrix membranes from graphitic carbon nitride nanosheets and polymers of intrinsic microporosity. *Journal Of Membrane Science*. Sep 15 2016;514:15-24.
22. Lotsch BV, Doeblinger M, Sehnert J, et al. Unmasking melon by a complementary approach employing electron diffraction, solid-state NMR spectroscopy, and theoretical calculations-structural characterization of a carbon nitride polymer. *Chemistry-a European Journal*. 2007 2007;13(17):4969-4980.
23. Wang Y, Wang X, Antonietti M. Polymeric Graphitic Carbon Nitride as a Heterogeneous Organocatalyst: From Photochemistry to Multipurpose Catalysis to Sustainable Chemistry. *Angewandte Chemie-International Edition*. 2012 2012;51(1):68-89.

24. Xin Q, Li Z, Li C, et al. Enhancing the CO₂ separation performance of composite membranes by the incorporation of amino acid-functionalized graphene oxide. *Journal Of Materials Chemistry A*. 2015 2015;3(12):6629-6641.
25. Zhou F, Tien HN, Xu WL, et al. Ultrathin graphene oxide-based hollow fiber membranes with brush-like CO₂-philic agent for highly efficient CO₂ capture. *Nature Communications*. Dec 13 2017;8.
26. Niu P, Zhang L, Liu G, Cheng H-M. Graphene-Like Carbon Nitride Nanosheets for Improved Photocatalytic Activities. *Advanced Functional Materials*. Nov 21 2012;22(22):4763-4770.
27. Sing KSW, Everett DH, Haul RAW, et al. REPORTING PHYSISORPTION DATA FOR GAS SOLID SYSTEMS WITH SPECIAL REFERENCE TO THE DETERMINATION OF SURFACE-AREA AND POROSITY (RECOMMENDATIONS 1984). *Pure And Applied Chemistry*. 1985 1985;57(4):603-619.
28. Peng Y, Li Y, Ban Y, et al. Metal-organic framework nanosheets as building blocks for molecular sieving membranes. *Science*. Dec 12 2014;346(6215):1356-1359.
29. Zhang X, Xie X, Wang H, Zhang J, Pan B, Xie Y. Enhanced Photoresponsive Ultrathin Graphitic-Phase C₃N₄ Nanosheets for Bioimaging. *Journal Of the American Chemical Society*. Jan 9 2013;135(1):18-21.
30. Ma TY, Tang Y, Dai S, Qiao SZ. Proton-Functionalized Two-Dimensional Graphitic Carbon Nitride Nanosheet: An Excellent Metal-/Label-Free Biosensing Platform. *Small*. Jun 25 2014;10(12):2382-2389.
31. Liu L, Zhou Y, Xue J, Wang H. Enhanced anti-pressure ability through graphene oxide membrane by intercalating g-C₃N₄ nanosheets for water purification. *AIChE Journal*. 2019.
32. Yang S, Gong Y, Zhang J, et al. Exfoliated Graphitic Carbon Nitride Nanosheets as Efficient Catalysts for Hydrogen Evolution Under Visible Light. *Advanced Materials*. May 7 2013;25(17):2452-2456.
33. Zhang D, Guo Y, Zhao Z. Porous defect-modified graphitic carbon nitride via a facile one-step approach with significantly enhanced photocatalytic hydrogen evolution under visible light irradiation. *Applied Catalysis B-Environmental*. Jun 15 2018;226:1-9.
34. Wang Y, Liu L, Xue J, Hou J, Ding L, Wang H. Enhanced water flux through graphitic carbon nitride nanosheets membrane by incorporating polyacrylic acid. *AIChE Journal*. 2018;64(6):2181-2188.
35. Thankamony RL, Li X, Das SK, Ostwal MM, Lai Z. Porous covalent triazine piperazine polymer (CTPP)/PEBAX mixed matrix membranes for CO₂/N₂ and CO₂/CH₄ separations. *Journal Of Membrane Science*. Dec 1 2019;591.
36. Wijmans JG, Baker RW. THE SOLUTION-DIFFUSION MODEL - A REVIEW. *Journal Of Membrane Science*. Nov 15 1995;107(1-2):1-21.
37. Shen J, Liu G, Huang K, Chu Z, Jin W, Xu N. Subnanometer Two-Dimensional Graphene Oxide Channels for Ultrafast Gas Sieving. *Acs Nano*. Mar 2016;10(3):3398-3409.
38. Murali RS, Ismail AF, Rahman MA, Sridhar S. Mixed matrix membranes of Pebax-1657 loaded with 4A zeolite for gaseous separations. *Separation And Purification Technology*. May 29 2014;129:1-8.
39. Zheng Y, Wu Y, Zhang B, Wang Z. Preparation and characterization of CO₂-selective Pebax/NaY mixed matrix membranes. *Journal Of Applied Polymer Science*. Mar 5 2020;137(9).
40. Murali RS, Sridhar S, Sankarshana T, Ravikumar YVL. Gas Permeation Behavior of Pebax-1657 Nanocomposite Membrane Incorporated with Multiwalled Carbon Nanotubes. *Industrial & Engineering Chemistry Research*. Jul 21 2010;49(14):6530-6538.
41. Zhao D, Ren J, Wang Y, et al. High CO₂ separation performance of Pebax (R)/CNTs/GTA mixed matrix membranes. *Journal Of Membrane Science*. Jan 1 2017;521:104-113.

42. Long X, Pan Y, Zeng G, Jiang J, Wang C. Preparation of Poly(ether-block-amide)/Attapulgite Mixed Matrix Membranes for CO₂/N₂ Separation. *Journal of Membrane Science*. 2015;500:66-75.
43. Zhao D, Ren J, Qiu Y, et al. Effect of graphene oxide on the behavior of poly(amide-6-b-ethylene oxide)/graphene oxide mixed-matrix membranes in the permeation process. *Journal Of Applied Polymer Science*. Nov 5 2015;132(41).
44. Shen J, Zhang M, Liu G, Guan K, Jin W. Size Effects of Graphene Oxide on Mixed Matrix Membranes for CO₂ Separation. *Aiche Journal*. Aug 2016;62(8):2843-2852.
45. Li H, Tuo L, Yang K, et al. Simultaneous enhancement of mechanical properties and CO₂ selectivity of ZIF-8 mixed matrix membranes: Interfacial toughening effect of ionic liquid. *Journal Of Membrane Science*. Aug 1 2016;511:130-142.
46. Shen J, Liu G, Huang K, et al. UiO-66-polyether block amide mixed matrix membranes for CO₂ separation. *Journal Of Membrane Science*. Sep 1 2016;513:155-165.
47. Sutrisna PD, Hou J, Li H, Zhang Y, Chen V. Improved operational stability of Pebax-based gas separation membranes with ZIF-8: A comparative study of flat sheet and composite hollow fibre membranes. *Journal Of Membrane Science*. Feb 15 2017;524:266-279.
48. Sutrisna PD, Hou J, Zulkifli MY, et al. Surface functionalized UiO-66/Pebax-based ultrathin composite hollow fiber gas separation membranes. *Journal Of Materials Chemistry A*. Jan 21 2018;6(3):918-931.
49. Zhang X, Zhang T, Wang Y, et al. Mixed-matrix membranes based on Zn/Ni-ZIF-8-PEBA for high performance CO₂ separation. *Journal Of Membrane Science*. Aug 15 2018;560:38-46.
50. Duan K, Wang J, Zhang Y, Liu J. Covalent organic frameworks (COFs) functionalized mixed matrix membrane for effective CO₂/N₂ separation. *Journal Of Membrane Science*. Jan 15 2019;572:588-595.
51. Xie K, Fu Q, Xu C, et al. Continuous assembly of a polymer on a metal-organic framework (CAP on MOF): a 30 nm thick polymeric gas separation membrane. *Energy & Environmental Science*. Mar 1 2018;11(3):544-550.
52. Kim S, Hou J, Wang Y, et al. Highly permeable thermally rearranged polymer composite membranes with a graphene oxide scaffold for gas separation. *Journal of Materials Chemistry A*. 2018;6(17):7668-7674.
53. Lee J, Kim JS, Kim JF, et al. Densification-induced hollow fiber membranes using crosslinked thermally rearranged (XTR) polymer for CO₂ capture. *Journal of membrane science*. 2019;573:393-402.
54. Fu Q, Halim A, Kim J, et al. Highly permeable membrane materials for CO₂ capture. *Journal Of Materials Chemistry A*. 2013 2013;1(44):13769-13778.
55. Ji Y, Zhang M, Guan K, Liu G, Jin W, Zhao J. High-Performance CO₂ Capture through Polymer-Based Ultrathin Membranes. *Advanced Functional Materials*. Aug 2019;29(33).
56. Liu M, Xie K, Nothling MD, et al. Ultrathin Metal-Organic Framework Nanosheets as a Gutter Layer for Flexible Composite Gas Separation Membranes. *Acs Nano*. Nov 2018;12(11):11591-11599.